

Comparing the Electrochemical Performance of Silicon/N-Rich Carbon Composite-based Anode Material Prepared by Hot-drying and Freeze-drying methods

QiLiang Pan¹, Jianguo Zhao^{1,2,*}, Lihua Yao¹, Ning Li¹, Shang Jiang¹, Baoyan Xing^{1,2}, Wenshan Qu¹, Mingjun Pang¹, Rui Liu¹, Wei Liang²

¹ Institute of Carbon Materials Science, Shanxi DaTong University, DaTong, Shanxi province 037009; China

² College of Materials Science and Engineering, Taiyuan University of Technology, Taiyuan, Shanxi province 030024, China;

*E-mail: pql0204@163.com

Received: 1 December 2021 / Accepted: 25 January 2022 / Published: 4 March 2022

The cycle life and coulomb efficiency of silicon anode materials for lithium-ion batteries are greatly reduced due to the large volume change during charge-discharge process, which limits its commercial application. Herein, a silicon/N-rich carbon anode material was prepared by using N-rich gelatin as the raw material. Two different processing methods, hot-drying and freeze-drying, were adopted to prepare Si/C composite-based electrodes, (Si@GC-H and Si@GC-F). Compared with the traditional hot-drying method to prepare the Si@GC-H composite, the Si@GC-F composite showed good electrochemical performance by controlling the dispersibility of Si nanoparticles using hydrogel and gas gel. The Si@GC-F composite exhibited an even distribution of Si nanoparticles in the carbonaceous matrix, which prevented the agglomeration of Si nanoparticles. The specific discharge capacity of Si@GC-F composite (Si content is only 20.06%) was 528.1 mAh g⁻¹ after 100 cycles at the current density of 0.1 A g⁻¹, and the Coulombic efficiency was 99.7%. The specific capacity can fully meet the existing commercial cathode electrode matching.

Keywords: Li-ion battery; Silicon; Gelatin; Freeze drying; Composite;

1. INTRODUCTION

Lithium-ion batteries (LIBs) are extensively applied in portable tools and electronic products, like electric vehicles and the storage of electric power, etc., owing to their excellent properties[1, 2]. The currently commercialized anode material, graphite, has a theoretical specific capacity of 372 mAh g⁻¹ and an actual specific capacity close to the theoretical capacity, which limits its application in different fields[3]. Therefore, it is necessary to develop new-generation anode materials for LIBs featuring high

energy density, high cycling rate, and long cycle life. In contrast, silicon (Si) has a theoretical capacity of about ten times of graphite; and is, therefore, an ideal material to prepare the high-capacity electrodes[4, 5]. However, a significant decrease in the cycle life and Coulombic efficiency (CE) of Si electrodes is caused by the volume expansion of Si during the charge-discharge processes[6]. Such volume expansion can be effectively buffered by using different types of Si nanomaterials, like granular, tubular, linear, porous Si nanomaterials, etc.[2, 5, 7-11]. However, the high specific surface area of Si nanomaterials results in the formation of large solid electrolyte interface (SEI) membranes, which further causes a large irreversible capacity and a relatively low CE of these materials[12, 13]. For improving the electrochemical performance of Si materials, Si/carbon (C) composite-based anode materials can be prepared by wrapping Si with C, which buffers the volume change of Si during the charge-discharge processes and improves the electrical conductivity of Si-based materials[14].

The even dispersion of Si nanomaterials by carbonaceous materials is a critical factor in ensuring the outstanding performance of the Si/C anode materials. The aggregation of Si nanomaterials can be effectively avoided through evenly dispersing and wrapping the Si nanomaterials with the carbonaceous materials, and the electrochemical performance of the Si/C composite materials can be improved through doping with foreign atoms, such as N, P. Of these, N atoms are more helpful for the insertion of Li ions, as their electronegativity and binding capacity with Li-ions are relatively stronger than the C atoms[15]. Among various C sources, gelatin has the properties of dissolution under high temperature as well as at low temperature and may result in sufficient dispersion and fixation of the Si nanomaterials. Therefore, it is an ideal C source for preparing the Si/C composite-based anode materials. Gelatin is an amphoteric polyelectrolyte generated by the acid or alkali modification of collagen and is an N-rich substance. It is composed of three polymeric chains with a triple helix structure and has a molecular mass of about 300000. Apart from that, it is inexpensive and environmental-friendly merchandise. After gelatin is pyrolyzed, N atoms are trapped in the C-based material in the forms of pyridine N, pyrrole N, and graphitic N[15]. The high N content can effectively improve the electrochemical performance of Si/C composite materials. Shen et al.[13] used gelatin as the C source, and calcium carbonate (CaCO_3) as the pore former to prepare a porous C-based material; and then the porous carbonaceous material was mixed with silica and magnesium, and a porous Si/C composite material was obtained through the thermal reduction of Mg. Shi et al.[16] mixed gelatin with CaCO_3 and Si nanomaterial, and a porous Si/C composite material was obtained through carbonization and acid etching. According to the research findings, it is concluded that gelation can be used as the C source, and by using the special properties of gelatin, a Si/C composite-based anode material doped with highly dispersed N atoms can be produced, which provides new thinking for the preparation of anode materials for Li-ion batteries.

In this paper, gelatin is used as the raw material, and different processes like the gel method, freeze-drying, and carbonization method are combined to prepare the Si/N-rich C composite-based anode material. Process control is exercised to produce a porous C-based material in the absence of a pore former. The even dispersion of Si nanomaterials in the matrix is addressed, and the controlled dispersion of Si nanomaterials in the matrix is achieved. The microstructure and electrochemical performance of the Si/N-rich C composite-based anode material are evaluated using different characterization techniques. The properties of the Si/C composite-based anode material prepared by the proposed freeze-drying method are compared with that of the traditional hot-drying method.

2. EXPERIMENTAL

2.1 Preparation of the Si/N-rich C anode material

A beaker containing 50 mL of deionized water was placed in a water bath at 60 °C, and the deionized water was continuously stirred until 1.62 g gelatin was completely dissolved. The beaker with the above gelatin solution was placed in an ultrasonic cleaner. 0.1 g Si nanomaterial with particle size of 30-50nm was added, and the gelatin solution was ultrasonically treated for 1 h. After ultrasonic treatment, the suspension was continuously stirred with a magnetic stirrer at room temperature, which gradually turned into a hydrogel at a low temperature. In this way, the dispersion and fixation of Si nanomaterials were achieved. The hydrogel was placed in a freeze-dryer and was subjected to freeze-drying at a cold-strap temperature of -80 °C for 48 h. After freeze-drying, the hydrogel was turned into an aerogel with a fluffy structure. The frozen sample was placed in a tube heater and carbonized at 500 °C for 2 h under the argon ambiance. Thus a freeze-dried Si/N-rich C composite material (named Si@GC-F) was obtained, and the schematic diagram of the preparation method is shown in Figure 1. In a control test, the same steps were taken, except for the Si nanomaterials addition; thus, an N-rich carbonaceous material was obtained (named GC). In another controlled test, the same steps were taken. But in this case, the hydrogel was subjected to hot-drying at 80 °C for 12 h; and then the heated sample was placed in a tube heater and carbonized at 500 °C for 2 h under the argon ambiance. Thus a hot-drying Si/N-rich C composite material was obtained (named Si@GC-H).

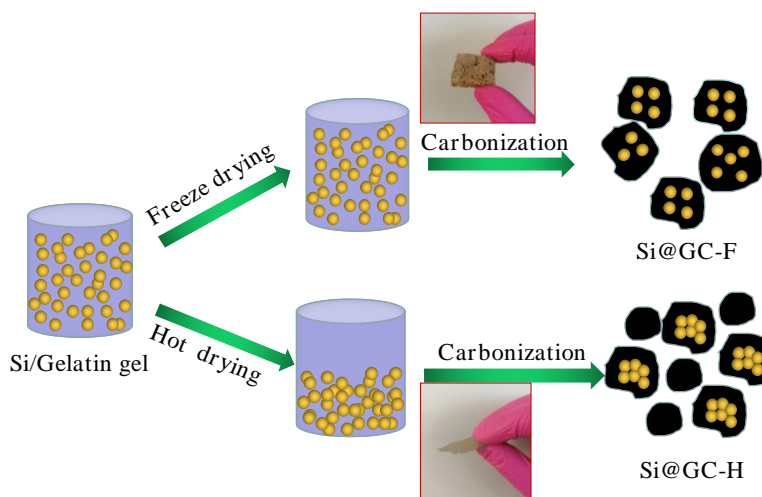


Figure 1. Schematic diagram of preparation of Si/N-rich C material

2.2 Structural characterization of the materials

The phase structure and crystal structure of the produced samples were characterized with the Bruker D8 Focus X-ray diffractometer (XRD, using Cu K α radiation, 30 kV voltage, and a scanning range of 10° – 80°). The morphology and microstructure were obtained with the field emission scanning electron microscope (SEM, TESCAN MAIA3) and the transmission electron microscope (TEM,

JEM2100F). The elemental composition was analyzed with the energy dispersive X-ray spectrometer (EDS, Oxford X-act). The surface elements and their valence states were analyzed with the X-ray photoelectron spectrometer (XPS, Thermo Scientific K- α spectrometer) under the monochromated Al K α radiation with an energy of 1486.68 eV. The specific surface area and pore size were analyzed with the nitrogen adsorbent (Micromeritics TriStar 3020). The component contents were analyzed with the thermogravimeter (TGA, Netzsch TA449F5) in the air atmosphere with the rate of increase in temperature of about 10 °C min⁻¹.

2.3 Electrochemical performance testing of the materials

The electrochemical performance of the electrode materials was tested with the half-cell. The active substance, acetylene black, and sodium alginate were mixed with deionized water in a mass ratio of 6:2:2. After cleaning the surface with ethanol, the obtained mixture was evenly applied onto a pure copper foil. The copper foil was placed in a vacuum dryer and dried at 100 °C for 24 h. Thus the working electrode was obtained. The working electrode was treated with the slicer and was cut into a circular electrode of 12 mm diameter. The circular electrode was placed on a slice press and was pressurized under a pressure of 10 MPa for 2-3 min. The button half-cell was assembled in a glove box under the high-purity argon ambiance (where the oxygen content and water content both were lower than 0.1 ppm). The pure Li foil with a diameter of 14 mm was used as the counter electrode, and the polyethylene microporous membrane with a diameter of 16 mm was used as the diaphragm. The mixture of ethylene carbonate, dimethyl carbonate, and ethyl carbonate (with a volume ratio of 1:1:1) as well as 5% fluoroethylene carbonate containing 1 mol/L lithium hexafluorophosphate was used as the electrolyte. The assembly sequence of the battery pack is as follows: anode shell—spring leaf—gasket—lithium foil—membrane—working electrode—cathode shell. For the battery pack, the cyclic voltammetry (CV) and electrochemical impedance spectroscopy (EIS) tests were conducted with the CHI660E electrochemical workstation. The cyclic voltammetry test was conducted in the voltage range of about 0.01 V-2 V with a scanning rate of 0.2 mV s⁻¹. The AC impedance data was recorded in the frequency range of 100 Hz-0.01 Hz at the AC voltage of 5 mV. The galvanostatic charge-discharge and rate performance tests were conducted with the CT2001A battery tester. The voltage range was 0.01 V-2 V, and the current densities in the rate performance test were 0.1 A g⁻¹, 0.2 A g⁻¹, 0.5 A g⁻¹, and 0.1 A g⁻¹.

3. RESULTS AND DISCUSSION

The SEM images of GC and the Si@GC-H and Si@GC-F composites are shown in Figure 2. The microstructure of GC shows an amorphous carbon morphology. Whereas, the composite material Si@GC-H shows a huge agglomeration of Si nanoparticles of 30-50 nm diameter, as well as the phase separation between Si nanoparticles and GC (Figure 2b). In contrast, for composite material Si@GC-F, there is an even distribution of Si nanoparticles in GC, as well as proper phase separation between Si nanoparticles and GC is seen, which prevents the agglomeration of Si nanoparticles. This phenomenon

can also be observed from the element mapping diagrams of the Si@GC-F and Si@GC-H composite materials, as shown in Figure 2d-e. For the composite material Si@GC-H, an uneven distribution of various elements is observed, especially of Si and C, which indicates that Si nanoparticles are not wrapped well with C. In contrast, for the Si@GC-F composite material, an even distribution of C, Si, and N, is observed, which indicates that Si nanoparticles are well wrapped by the N-rich C material obtained from the carbonized aerogel produced through freeze-drying, which prevented the agglomeration of Si nanoparticles effectively.

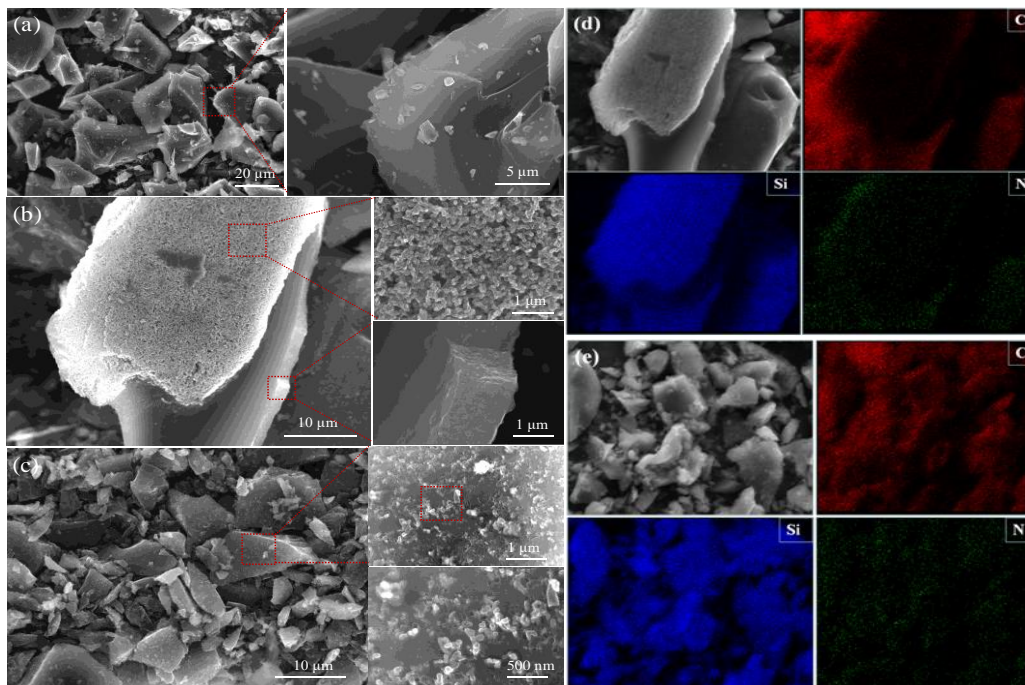


Figure 2. SEM images of GC (a), Si@GC-H (b) and Si@GC-F (c) composites. Elemental distribution of Si@GC-H (d) and Si@GC-F (e) composites

The TEM images of the Si@GC-F composite material are shown in Figure 3, and the distribution of Si nanoparticles in the gelatin carbon is further analyzed. As shown in the images, Si nanoparticles are evenly distributed in the C material, and there is not much agglomeration which indicates that Si nanoparticles are dispersed well and wrapped by the prepared N-rich C material. As shown in the high-resolution TEM image (Figure 3c), the interplanar distance of 0.31 nm is attributed to the crystal plane of Si (111). The selected area electron diffraction image (SAED) (Figure 3d) shows crystalline and non-crystalline diffraction pattern, which indicates that Si nanoparticles are wrapped with the amorphous C, where the characteristic crystalline diffraction rings are of Si (111), Si (220) and Si (311).

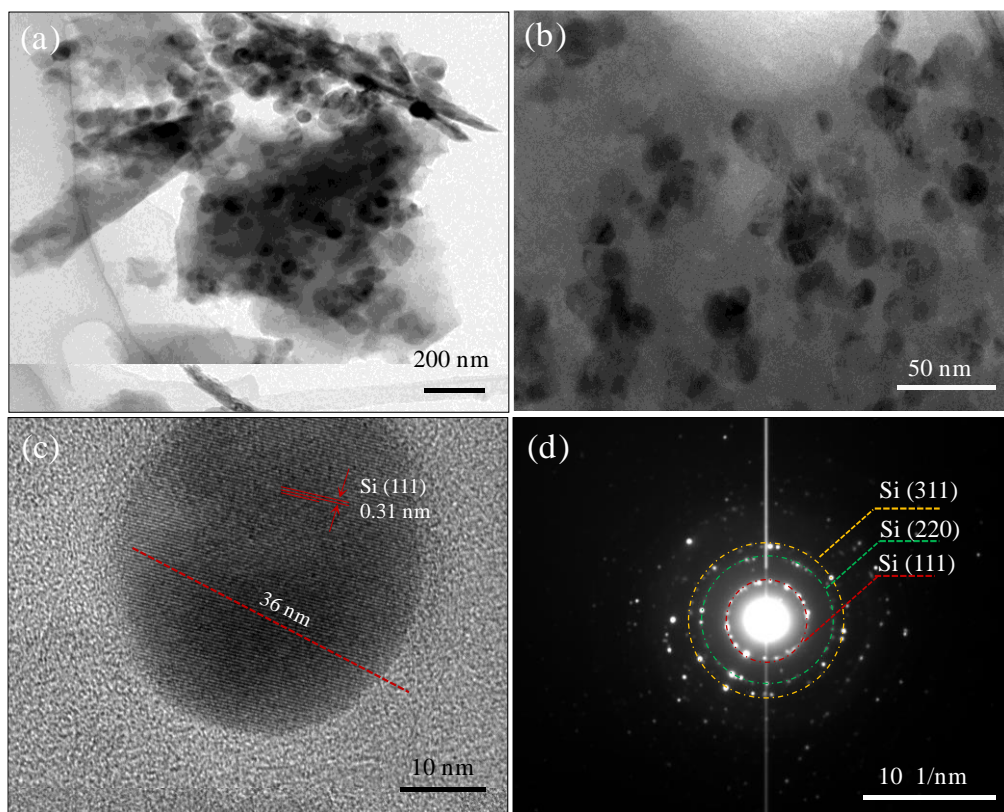


Figure 3. TEM (a, b) and HRTEM images (c) of Si@GC-F composite. The corresponding SAED pattern (d)

The EDS diagram of GC is shown in Figure 4a. As shown in the diagram, the main elements of the pyrolytic carbon are C, N, O, Na, and S. Of these, Na and S, which are the residues of the gelatin carbonization process, are relatively less. In the pyrolytic carbon, the elemental concentration of C is the highest, with a mass percent of 76.54%, followed by N, with a mass percent of 16.92%. Hence it can be said that N is an inherent component of the material, and with the even distribution of N, the electrochemical performance of the material can be substantially improved.

The XRD patterns of the GC and the Si@GC-H and Si@GC-F composite materials are shown in Figure 4b. As shown in the diagrams, for GC, the wide diffraction peak at 22.1° is attributed to the characteristic peak of pyrolytic amorphous carbon[17]. For the Si@GC-F and Si@GC-H composite materials, the diffraction patterns are composed of the characteristic peaks of amorphous carbon and crystalline Si, where the diffraction peaks at 28.53° , 47.38° , 56.25° , 69.30° and 79.54° are correlated with the crystal planes of Si (111), Si (220), Si (311), Si (400) and Si (331) (JCPDS 27–1402)[18].

The Raman spectra of the GC and the Si@GC-H and Si@GC-F composite materials are shown in Figure 4c. For the amorphous carbon material GC, the two absorption peaks at 1370 cm^{-1} and 1587 cm^{-1} correspond to the disordered D peak of amorphous carbon and the G peak of graphite, respectively. The D peak is correlated with the destruction of the symmetric hexagonal lattice of graphite, and the G peak is correlated with the symmetric stretching vibration of the C-C bond[19]. The graphitization degree is correlated with the peak strength; the greater the I_D/I_G value, the lower is the graphitization degree. For the Si@GC-F and Si@GC-H composite materials, the Raman spectra are composed of the

characteristic peaks of Si and the D peak and G peak of amorphous carbon. The absorption peak at 516 cm^{-1} is correlated with the optical phonon absorption of crystalline Si under the Si-Si stretching mode[20]. The I_D/I_G values of the Si@GC-F and Si@GC-H composite materials are found to be 0.83 and 0.80, respectively, which indicates that the carbon present in the two composite materials is composed of amorphous carbon with the short-range ordering and graphitic carbon with the long-range ordering, which may improve the electrical conductivity of the anode material[21]. The absorption peak at 516 cm^{-1} of the Si@GC-H composite material is lower than that of the Si@GC-F composite material, which may be a manifestation of the uneven distribution of Si nanoparticles in the pyrolytic carbon and a low Si content.

The thermogravimetric analysis curves of GC, the Si@GC-H, and Si@GC-F composite materials obtained in the air atmosphere from room temperature to $900\text{ }^\circ\text{C}$ are shown in Figure 4d. In the temperature range of $80\text{ }^\circ\text{C}$ - $100\text{ }^\circ\text{C}$, there is an initial decomposition of 3.96%, which is attributed to material dewatering. In the temperature range of $400\text{ }^\circ\text{C}$ - $700\text{ }^\circ\text{C}$, there is a remarkable weight loss of the three materials, which is attributed to carbon oxidation in the air atmosphere. In the temperature range above $700\text{ }^\circ\text{C}$, there is complete decomposition of carbon components. In the temperature range above $800\text{ }^\circ\text{C}$, the weight gain of the Si@GC-F and Si@GC-H composite materials occurs, which is attributed to the surface oxidation of Si to SiO_x [22]. According to the results of the thermogravimetric analysis, the Si contents of the Si@GC-F and Si@GC-H composite are about 20.06% and 10.10%, respectively. The observed difference in Si content between the two composite materials is consistent with the obtained results. Under the same processing condition (addition of Si nanomaterials), the Si@GC-H composite material obtained through the traditional hot-drying method shows a relatively more amount of unwrapped Si nanoparticles by gelatin, as detected by the thermogravimetric testing process. This might be due to the uneven distribution of Si nanoparticles, resulting in higher carbon content and a relatively lower Si content in the composite material, which may affect the electrochemical performance of the composite material.

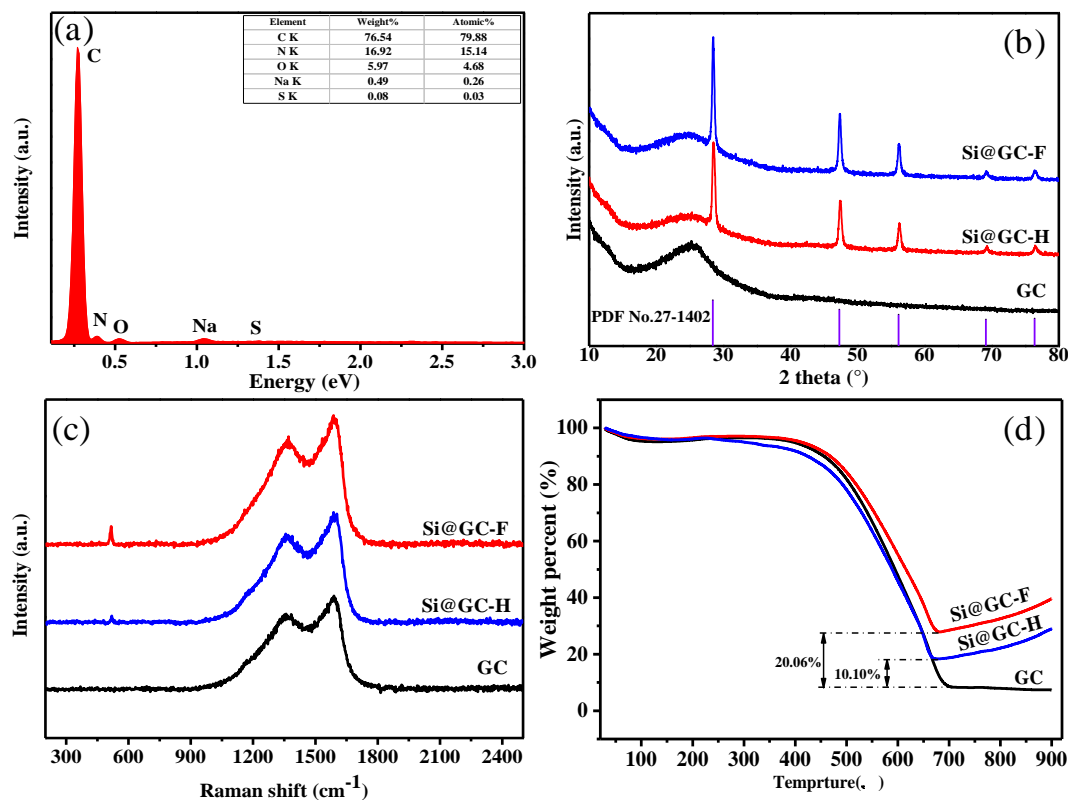


Figure 4. EDS of GC (a). The XRD patterns (b), Raman spectra(c) and Thermogravimetric curve(d) of GC, Si@GC-F and Si@GC-H composites.

The isotherm and pore size distribution diagrams of GC and the Si@GC-H and Si@GC-F composites are shown in Figure 5a, b. According to the IUPAC classification, the curves of the three samples are IV(a)-type isotherm adsorption/desorption curves[23]. Analyzing the specific surface area with the Brunauer-Emmett-Teller (BET) method, the specific surface areas of GC and the Si@GC-H and Si@GC-F composites were found, which are about 27.23 m² g⁻¹, 53.46 m² g⁻¹ and 69.70 m² g⁻¹, respectively. The specific surface area of the Si@GC-F composite material is larger than that of the Si@GC-H composite, which indicates that for the three-dimensional structure obtained through freeze-drying, there are good channels of Li⁺ transfer. The pore size distribution was evaluated by the Barrett-Joyner-Halenda (BJH) model. As shown in Figure b, the pore size distribution of Si@GC-F composite is wider than that of Si@GC-H composite, and the special pore structure of the former is helpful for the diffusion of Li⁺ and improvement of the electrochemical performance of electrodes.

The XPS spectra of the surface chemical composition and elemental valence states of the Si@GC-F composite are shown in Figure 5c-f. As shown in the figure(Figure 5c), binding energies of 102.7 eV, 284.8 eV, 399.8 eV, and 533.1 eV are correlated with Si 2p, C 1s, N 1s, and O 1s, respectively. In the high-definition C 1s spectrum (Figure 5d), two characteristic peaks are detected through the fitting. The peak at binding energy 284.8 eV is attributed to the graphitic carbon with sp² hybridization, which indicates that most carbon atoms are located in the conjugated honeycomb lattice, and the peak at binding energy 285.9 eV is correlated to C-N bonding[24, 25]. In the high-definition Si 2p spectrum (Figure 5e), the two characteristic peaks appearing at binding energies of 99.8 eV and 102.8 eV are correlated with

Si-Si bonding and Si-O bonding, respectively. The formation of the Si-O bond is mainly attributed to the Si surface oxide layer formed under high temperatures[26]. In the high-definition N 1s spectrum (Figure 5f), three characteristic peaks are detected through the fitting. The peaks at binding energies of 398.5 eV, 400.4 eV, and 402.4 eV are correlated with pyridine N, pyrrole N, and graphitic N, respectively[27]. Of these, the pyridine N is formed by replacing one carbon atom from the six-carbon ring, bonding with two sp^2 carbon atoms; and is able to provide one pair of lone-pair electrons by serving as the electron donor. Pyrrole N is the N atom on the five-carbon ring. Graphitic N is formed by bonding with three sp^2 carbon atoms and can be doped in the graphitized carbon plane. It is able to provide positive charges and serves as the electron acceptor. The N-rich C material can effectively improve the electrical conductivity of the electrode materials owing to its high charge transfer capacity and can improve the Li^+ storage capacity due to the additional insertion sites of Li^+ , which are formed due to the numerous defects caused by N doping.

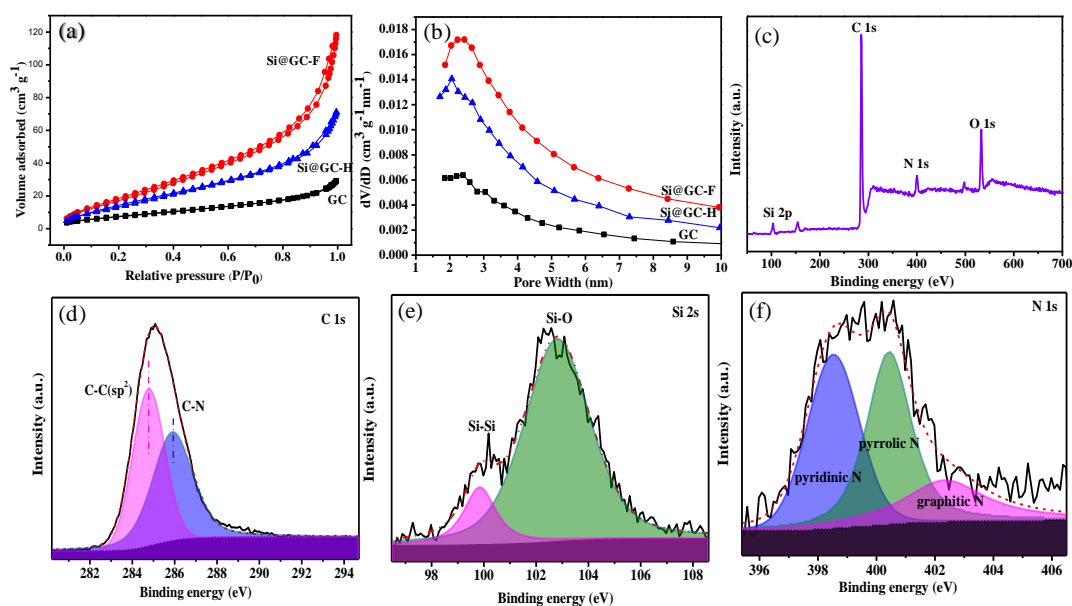


Figure 5. N_2 adsorption/desorption isotherms curves (a) and the pore size distribution curves (b) of GC, Si@GC-F and Si@GC-H composite. Survey (c) and high-resolution XPS of C 1s (d), Si 2p (e) and N 1s (f) of Si@GC-F composite

To examine the electrochemical performance, the CV curves of pure Si, GC, and the Si@GC-F and Si@GC-H composites, are recorded for the first five cycles with a scanning rate of 0.2 mV s^{-1} , and the results are shown in Figure 6(a-d). As shown in the CV curve of pure Si (Figure 6a), during the initial Li^+ insertion process, the peak appears at 1.0 V, which is attributed to the formation of solid electrolyte membrane (SEI). This is the main cause of the irreversible capacity of pure Si. The reduction peak at 0.19 V is the formation peak of Si-Li alloy. The oxidation peaks at 0.32 V and 0.53 V are attributed to the delithiation of Si-Li alloy. As shown in the CV curve of GC (Figure 6b), during the first discharge process, the reduction peak appearing at about 1.0 V is correlated with the decomposition of electrolyte

and the formation of SEI[28]. The formation of SEI membranes can also be observed from the CV curves of the composite materials (Si@GC-F and Si@GC-H). The reduction peak at 0.2 V-0.01 V is correlated with the formation of non-crystalline Si-Li alloy, in which Li^+ is inserted into the crystalline Si. In the cathode scanning process, the oxidation peaks appearing at 0.32 V and 0.53 V are attributed to the transformation of the non-crystalline Si-Li alloy to non-crystalline Si. After the first cycle, the shapes of the CV curves repeat, but the area of the CV curves gradually increases, which is attributed to the activation of the electrode materials, in which more and more Si-Li alloy is formed from Li^+ and Si, and the Li insertion process is completed.

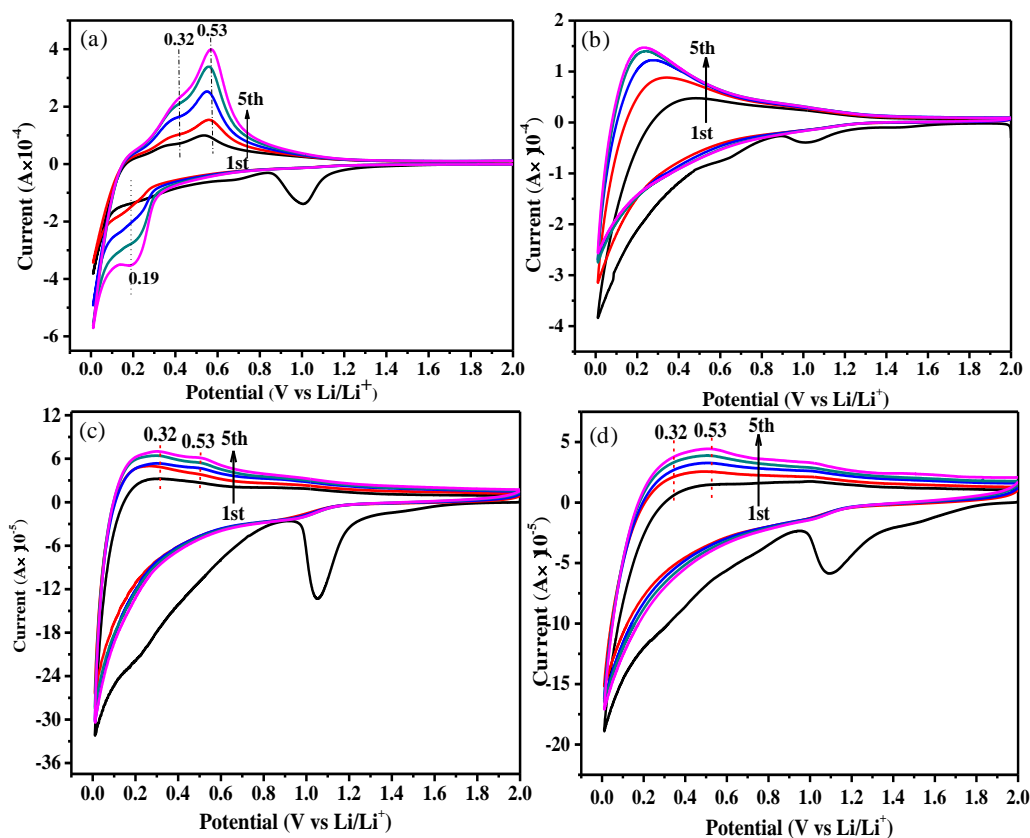


Figure 6. The CV curves pure Si (a), GC (b), Si@GC-H (c) and Si@GC-F (d) composites

The cycle performance curves of GC, pure Si, and the Si@GC-H and Si@GC-F composites are shown in Figure 7(a, b). The initial Coulombic efficiencies of GC, pure Si, and the electrode material Si@GC-H are 36.48%, 56.20%, and 45.64%, respectively. In contrast, the initial CE of the electrode material Si@GC-F is relatively high, about 60.74%. It is seen that, for electrode material Si@GC-F obtained through freeze-drying, the irreversible capacity is decreased. At the current density of 0.1 A g^{-1} , the specific discharge capacity of commercial Si nanomaterial-based electrode material is about 228.0 mAh g^{-1} after 50 cycles. The specific discharge capacity of GC is about 230 mAh g^{-1} after 100 cycles, but the initial CE is relatively low. The initial CE of the composite material Si@GC-H is also relatively low, the CE in the second cycle is only 92%, and the specific discharge capacity is about 433.0 mAh g^{-1}

¹, after 100 cycles. In contrast, the initial CE of the Si@GC-F composite is relatively high, and the CE in the second cycle is 98.8%, and the specific discharge capacity is about 528.1 mAh g⁻¹, after 100 cycles, and the charge-discharge efficiency is 99.6%. It is observed that for the Si@GC-H composite obtained through hot-drying, wrapping of Si nanoparticles by the N-rich C material improves the cycle performance, whereas poor initial efficiency is due to the extensive agglomeration of Si nanoparticles. In contrast, for the Si@GC-F composite reated through freeze-drying and carbonization, Si nanoparticles are evenly wrapped and dispersed, and the irreversible capacity is substantially decreased due to the absence of extensive agglomeration of Si nanoparticles. The cycle performance is good as a result of the formation of stable SEI.

The rate performances of GC, pure Si, and the Si@GC-H and Si@GC-F composites at different current densities are shown in Figure 7(c). As shown in the figure, the specific capacities of the four electrode materials are found to decrease significantly as the current density increases. Of these, the specific capacity of pure Si is found to decrease very significantly as the current density increases. The specific discharge capacity of pure Si after five cycles is about 1384.3 mAh g⁻¹ at the current density of 0.1 A g⁻¹. The specific discharge capacity is decreased to 379.7 mAh g⁻¹ at the current density of 0.5 A g⁻¹. When the current density is restored to 0.1 A g⁻¹, the specific discharge capacity is restored to 507.5 mAh g⁻¹. For GC, when the current densities are 0.1 A g⁻¹, 0.2 A g⁻¹ and 0.5 A g⁻¹, the specific discharge capacities are 427.2 mAh g⁻¹, 256.1 mAh g⁻¹, 177.0 mAh g⁻¹, respectively. When the current density is restored to 0.1 A g⁻¹, the specific discharge capacity is restored to 348.8 mAh g⁻¹. For the Si@GC-H composite, when the current density is 0.1 A g⁻¹, the specific discharge capacity after five cycles is about 487.3 mAh g⁻¹, which is similar to that of GC. Hence, it can be said that the rate performance of the Si@GC-H composite material is similar to that of GC. The main reasons are as follows: Si nanoparticles are not wrapped well with the gelatin carbon, and the constituent components of the electrode material are unevenly distributed, so the rate performance of the electrode material is unstable. However, the rate performance of the Si@GC-F composite is better than that of the Si@GC-H composite. The specific discharge capacities of the Si@GC-F composite are 1095.5 mAh g⁻¹, 894.4 mAh g⁻¹, and 577.9 mAh g⁻¹ at the current of 0.1 A g⁻¹, 0.2 A g⁻¹, and 0.5 A g⁻¹, respectively. The specific discharge capacity is restored to 929.2 mAh g⁻¹ at the current density of 0.1 A g⁻¹. Hence, it is seen that no structural damage is caused to the composite material by the large current, which is applied during the rate performance testing process (step-by-step). The superior rate of performance is attributed to the microstructure and the high N content of the electrode material.

The electrochemical impedance spectra of GC, pure Si, Si@GC-H, and Si@GC-F composite electrodes were examined to analyze the electrochemical performance of the materials, and the results are shown in Figure 7(d). The impedance data were fitted with the equivalent circuits illustrated in Figure 7(d). The Nyquist diagrams of the four electrodes are found to have similar characteristics, taking the shape of a semi-circle in the high-frequency area and an oblique line in the low-frequency area. The semi-circle in the high-frequency area is mainly attributed to the ohmic resistance and charge-transfer resistance, and the oblique line in the low-frequency area is attributed to Li⁺ diffusion in the electrodes[29]. In the equivalent circuits, R_e is the ohmic resistance (the sum of the electrolyte resistance, membrane resistance, and contact resistance); and R_{ct} and Q₂ are the discharge-transfer resistance at the boundary and the double-layer capacitor between the electrode and the electrolyte, respectively. The

Warburg impedance (Z_w) is attributed to Li^+ diffusion. As shown in the fitting results (Table 1), the discharge-transfer resistance (R_{ct}) of the Si@GC-F composite electrode is the lowest (43.34Ω), which indicates that a stronger discharge-transfer capacity is achieved due to its special microstructure.

The Li^+ diffusion coefficient (D_{Li}) was examined to analyze the Li^+ diffusion rate in the electrodes [18] and was calculated with the formula (1). As shown in formula (1), D_{Li} is inversely proportional to σ^2 (R is the gas constant, T is the absolute temperature, A is the surface area of the electrode, n is the number of the transferred electrons involved in the chemical reaction, F is the Faraday constant, C is the Li^+ concentration in the electrode, ω is the angular frequency, and σ is the Warburg factor). As shown in formula (2), the σ value is equal to the slope of the straight line of the $Z''-\omega^{-1/2}$ plot in the low-frequency area. The straight lines of the $Z''-\omega^{-1/2}$ plot in the low-frequency area of the electrodes are shown in Figure 7 (e). Through comparative analysis, it is seen that the slope of the Si@GC-F composite electrode is the smallest, which indicates that the Li^+ diffusion coefficient is the largest and the Li^+ diffusion rate is the highest in the electrode [30, 31]. The comprehensive analysis suggests that, for the composite material Si@GC-F, obtained through freeze-drying and carbonization, the even wrapping of Si nanomaterials with C material decreases the electrode resistance and increases the charge-transfer rate. The carbonized aerogel has a special spatial structure, which provides good channels for Li^+ diffusion and enables superior electrochemical performance.

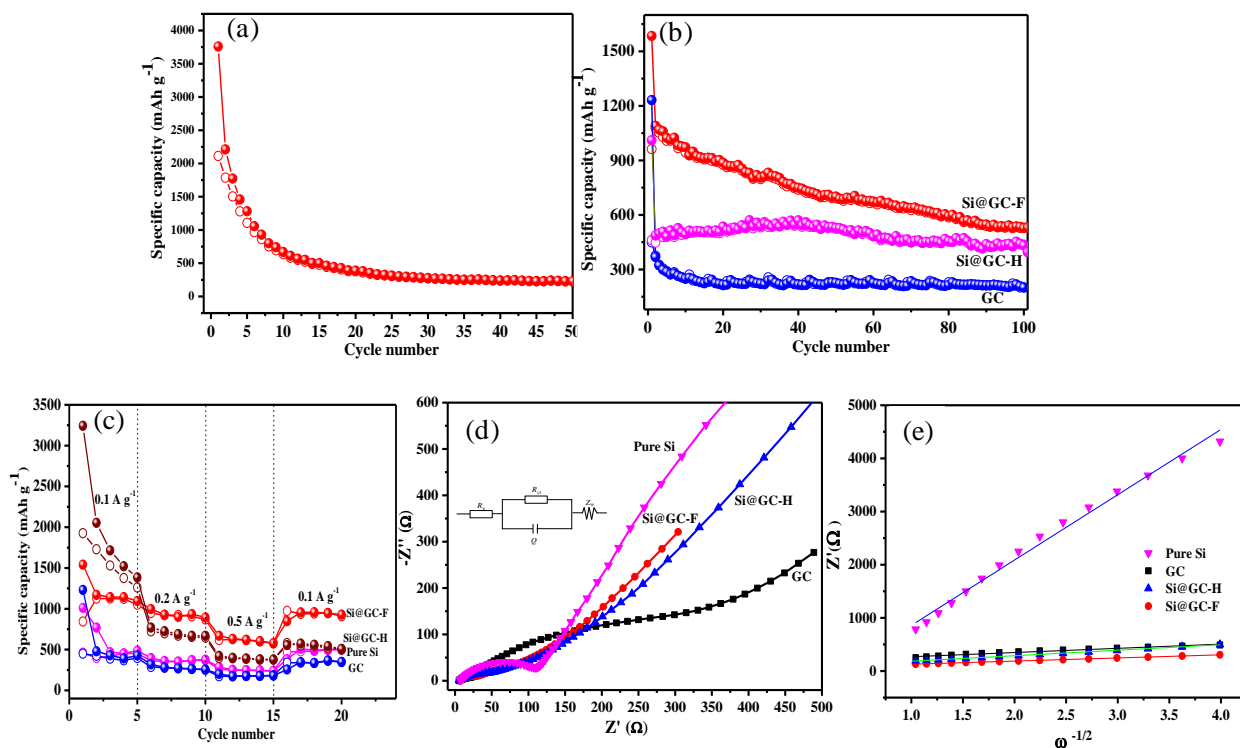


Figure 7. The cycle performance of pure Si (a) and GC, Si@GC-H, Si@GC-F composites (b). Rate performance (c) and Nyquist plots after 100 cycles (d) of GC, Si@GC-H and Si@GC-F electrodes. The equivalent circuit (inset). The relationship Z'' versus $\omega^{-1/2}$ at low frequency region (e)

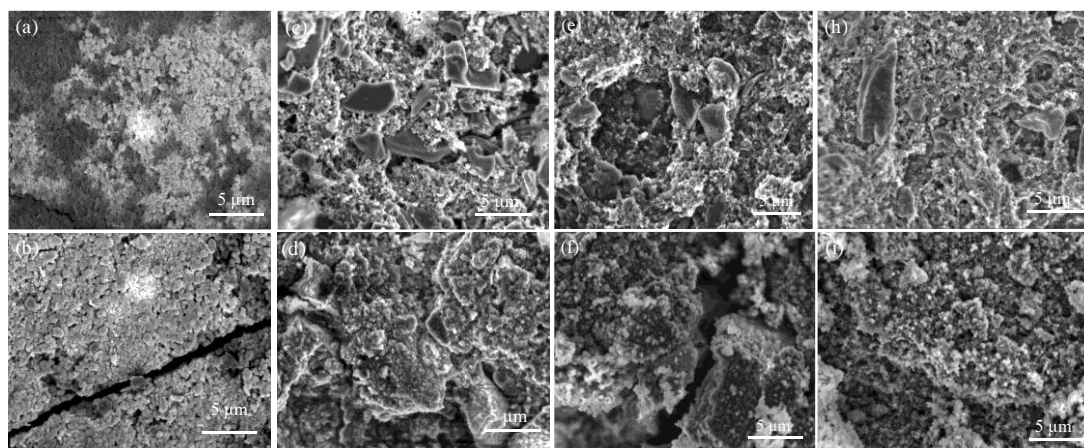
Table 1. Equivalent circuit parameters derived using equivalent circuit model

Electrodes	Pure Si	GC	Si@GC-H	Si@GC-F
R_e (Ω)	6.980	4.992	4.253	7.080
R_{ct} (Ω)	122.6	31.33	85.95	43.34

$$D_{Li} = \frac{R^2 T^2}{2A^2 n^4 F^4 C^2 \sigma^2} \quad (1)$$

$$Z' = R_e + R_{ct} + \sigma \omega^{-1/2} \quad (2)$$

The microstructures of pure Si, GC, Si@GC-H, and Si@GC-F electrodes are characterized before and after 100 the cycles, as shown in Figure 8. By the comparative analysis, it is seen that the morphologies of the four electrodes are in good order before the cycles, and the active substances and conductive agents are evenly diffused, maintaining a good coherence. After 100 cycles, large cracks are detected on the electrode surface in the pure Si and the Si@GC-H composite electrode, which indicates a remarkable volume change of Si nanoparticles during multiple Li^+ insertions, which damages the structure of the electrode surface. This is a manifestation of the unstable electrochemical performance of the two electrodes. For the GC and Si@GC-F-based electrodes, no remarkable structural changes are detected on the electrode surface, which indicates that the volume changes are effectively restrained in these two electrodes. For the Si@GC-F composite electrode, Si nanomaterials swelling is very effectively buffered by the even wrapping and dispersion of Si nanomaterials by the pyrolytic carbon. This improves the performance of the freeze-dried composite material.

**Figure 8.** SEM images of pure Si (a, b), GC (c, d), Si@GC-H (e, f) and Si@GC-F (h, i) electrodes before and after 100 cycles

The schematic diagram of the lithiation process is shown in Figure 9. For nanomaterials,

agglomeration is a very common phenomenon that occurs due to their high surface energy. In the preparation process, agglomeration is often reduced with the ultrasonic dispersion or high-speed string so that nanomaterials are sufficiently dispersed in the dispersion. However, in the subsequent standing and drying processes, agglomeration is resumed by the sedimentation of nanomaterials as a result of gravity and molecular motions. In view of this problem, in this paper, N-rich gelatin was used as the raw material. At first, Si nanoparticles were evenly dispersed in gelatin solution through ultrasonic treatment. The gelatin was gradually turned into a hydrogel through the temperature-controlled process, and Si nanoparticles were evenly bonded in the hydrogel. The hydrogel was freeze-dried in a freeze-dryer, gradually turned into an aerogel with a loose structure during the sublimation process, and Si nanoparticles were evenly dispersed by the gelatin. Then, the aerogel was carbonized to obtain a Si/N-rich C anode material with a spatial network structure. The freeze-drying and high-temperature carbonization treatments were combined to prepare the composite materials with evenly dispersed Si nanoparticles, which provide the buffer space for Si swelling. In contrast, in the hot-drying treatment, gelatin was continuously dissolved under a high temperature, so the phase separation occurred by the sedimentation of Si nanoparticles as a result of gravity and molecular motions. In the subsequent carbonization process, large aggregates of Si nanoparticles (not wrapped by C) and pure carbon particles were obtained. In the Li insertion process, a change in volume was caused by the swelling of agglomerated Si nanoparticles, and surface cracks and unstable SEI membranes were created. Hence, the electrochemical performance of the composite material was seriously affected.

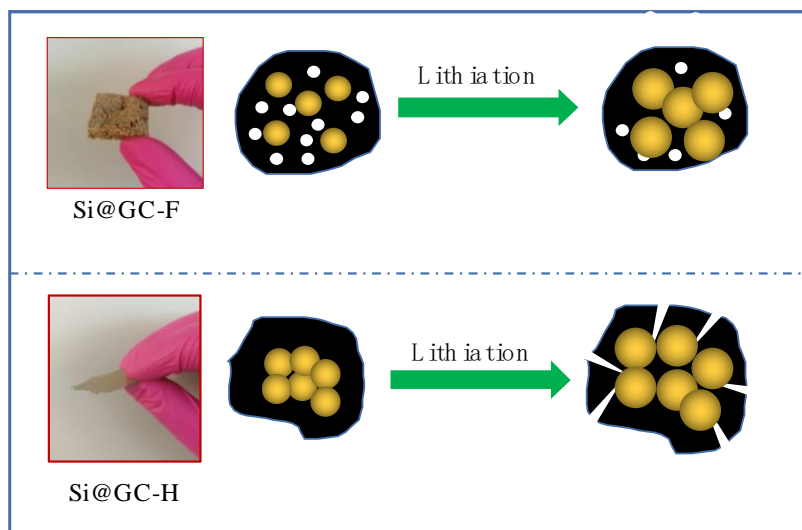


Figure 9. Schematic diagram of Si@GC-H and Si@GC-F composites before and after lithiation

4. CONCLUSION

In this paper, N-rich gelatin was used as the raw material, and process control was exercised to obtain hydrogel and aerogel, and then N-rich Si@GC-F composite material was obtained through freeze-

drying and carbonization. The Si@GC-F composite exhibit superior electrochemical properties with a specific discharge capacity of 528.1 mAh g⁻¹ after 100 cycles and CE of 99.7% at the current density of 0.1 A g⁻¹. The electrochemical performance was attributed to the even dispersion and wrapping of Si nanomaterials by the gelatin carbon, which provided a buffer space for Si swelling. The supply of abundant N by the gelatin carbon took the forms of pyridine N, pyrrole N, and graphitic N, which played a positive role in improving the Li storage performance and electrical conductivity of the composite material.

ACKNOWLEDGEMENT

This work was supported by the fund for National Natural Science Foundation of China (52071192), Shanxi collaborative innovation center of graphene development and application, Science and technology Innovation project of Higher education institutions in Shanxi Province (2021L389), Doctoral Research project of Datong University.

References

- 1 J.M. Tarascon, M. Armand, *Nature*, 414 (2001) 359.
- 2 C.K. Chan, R.N. Patel, M.J. O'Connell, B.A. Korgel, C. Yi, *ACS Nano*, 4 (2010) 1443.
- 3 R. Teki, M.K. Datta, R. Krishnan, T.C. Parker, T.M. Lu, P.N. Kumta, N. Koratkar, *Small*, 5 (2010) 2236.
- 4 H. Jia, P.F. Gao, J. Yang, J.L. Wang, Y.N. Nuli, Z. Yang, *Adv. Energy Mater.*, 1 (2011) 1036.
- 5 C. Martin, O. Crosnier, R. Retoux, D. Bélanger, D.M. Schleich, T. Brousse, *Adv. Funct. Mater.*, 21 (2011) 3524.
- 6 H. Xiang, K. Zhang, G. Ji, J.Y. Lee, C. Zou, X. Chen, J. Wu, *Carbon*, 49 (2011) 1787.
- 7 M. Ge, J. Rong, X. Fang, A. Zhang, Y. Lu, C. Zhou, *Nano Res.*, 6 (2013) 174.
- 8 Z. Wen, G. Lu, S. Mao, H. Kim, S. Cui, K. Yu, X. Huang, P.T. Hurley, O. Mao, J. Chen, *Electrochem. Commun.*, 29 (2013) 67.
- 9 H. Kim, M. Seo, M.H. Park, J. Cho, *Angew. Chem. Int. Ed.*, 49 (2010) 2146.
- 10 Z. Bao, M.R. Weatherspoon, S. Shian, Y. Cai, P.D. Graham, S.M. Allan, G. Ahmad, M.B. Dickerson, B.C. Church, Z. Kang, H.W. Abernathy, C.J. Summers, M. Liu, K.H. Sandhage, *Nature*, 446 (2007) 172.
- 11 M.S. Wang, L.Z. Fan, M. Huang, J.H. Li, X.H. Qu, *J. Power Sources* 219 (2012) 29.
- 12 L. Qie, W. Chen, H. Xu, X. Xiong, Y. Jiang, F. Zou, X. Hu, Y. Xin, Z. Zhang, Y. Huang, *Energy Environ. Sci.*, 6 (2013) 2497.
- 13 X. Shen, D. Mu, S. Chen, B. Xu, B. Wu, F. Wu, *J. Alloys Compd.*, 552 (2013) 60.
- 14 J. Lu, Z. Chen, F. Pan, Y. Cui, K. Amine, *Electrochem. Energy Rev.*, 1 (2018) 35.
- 15 Y. Mao, H. Duan, B. Xu, L. Zhang, Y. Hu, C. Zhao, Z. Wang, L. Chen, Y. Yang, *Energy Environ. Sci.*, 5 (2012) 7950.
- 16 L. Shi, W. Wang, A. Wang, K. Yuan, Z. Jin, Y. Yang, *J. Mater. Chem. A*, 3 (2015) 18190.
- 17 C.F. Zhang, R.X. Yu, T.F. Zhou, Z.X. Chen, H.K. Liu, Z.P. Guo, *Carbon*, 72 (2014) 169.
- 18 S. Chen, Z. Chen, X. Xu, C. Cao, M. Xia, Y. Luo, *Small*, 14 (2018) 1703361.
- 19 H. Tang, J.P. Tu, X.Y. Liu, Y.J. Zhang, S. Huang, W.Z. Li, X.L. Wang, C.D. Gu, *J. Mater. Chem. A*, 2 (2014) 5834.
- 20 J.P. Yang, Y.X. Wang, S.L. Chou, R.Y. Zhang, Y.F. Xu, J.W. Fan, W.X. Zhang, K.H. Liu, D.Y. Zhao, D.S. Xue, *Nano Energy*, 18 (2015) 133.
- 21 X.Y. Zhou, J.J. Tang, J. Yang, J. Xie, L.L. Ma, *Electrochim. Acta*, 87 (2013) 663.
- 22 M.S. Wang, L.Z. Fan, *J. Power Sources*, 244 (2013) 570.

- 23 M. Thommes, K. Kaneko, A.V. Neimark, J.P. Olivier, F. Rodriguez-Reinoso, J. Rouquerol, K.S.W. Sing, *Pure Appl. Chem.*, 87 (2015) 1051.,
- 24 D. Wei, Y. Liu, Y. Wang, H. Zhang, L. Huang, G. Yu, *Nano Lett.*, 9 (2009) 1752.
- 25 J.W. Jang, C.E. Lee, S.C. Lyu, T.J. Lee, C.J. Lee, *Appl. Phys. Lett.*, 84 (2004) 2877.
- 26 Z.L. Xu, B. Zhang, J.K. Kim, *Nano Energy*, 6 (2014) 27.
- 27 H.W. Kim, D.J. Lee, H. Lee, J. Song, H.T. Kim, J.K. Park, *J. Mater. Chem. A*, 2 (2014) 14557.
- 28 D. Ji, Y. Wan, Z. Yang, C. Li, G. Xiong, L. Li, M. Han, R. Guo, H. Luo, *Electrochim. Acta*, 192 (2016) 22.
- 29 W. Sun, R. Hu, M. Zhang, J. Liu, M. Zhu, *J. Power Sources*, 318 (2016) 113.
- 30 F.H. Du, B. Li, W. Fu, Y.J. Xiong, K.X. Wang, J.S. Chen, *Adv. Mater.*, 26 (2014) 6145.
- 31 H. Wu, G. Chan, J.W. Choi, I. Ryu, Y. Yao, M.T. McDowell, S.W. Lee, A. Jackson, Y. Yang, L. Hu, *Nat. Nanotechnol.*, 7 (2012) 310.

© 2022 The Authors. Published by ESG (www.electrochemsci.org). This article is an open access article distributed under the terms and conditions of the Creative Commons Attribution license (<http://creativecommons.org/licenses/by/4.0/>).